Influence of nonparabolic-energy-band dispersion on the optical constants close to the fundamental absorption in PbSe and $Pb_{1-x}Mn_xSe$ epitaxial films

Heinz Krenn, Shu Yuan,* Norbert Frank, and Günther Bauer
Institut für Halbleiterphysik, Johannes Kepler Universität, A-4040 Linz, Austria
(Received 21 July 1997)

The absorption and refractive indices of IV–VI semiconductor PbSe and $Pb_{1-x}Mn_xSe$ ($x \leqslant 0.013$) epitaxial layers are strongly influenced by band nonparabolicity in the absorbing regime above the fundamental energy gap E_g, as well as below in the transparent regime. This fact follows simply from causality since interband transitions far above the energy gap contribute remarkably to the optical constants *near* and *below* E_g. The observation of multiple reflection and interference phenomena in the transmission spectrum of the epitaxial layers grown on BaF_2 substrates, which were taken with high photometric accuracy (0.1%), allowed us to probe the dispersion of the refractive index very precisely as well as to determine the energy gap of PbSe and $Pb_{1-x}Mn_xSe$ with an uncertainty of ± 2 meV. A dielectric function is derived which contains the contributions from the interband transitions at the L point of the Brillouin zone and the residual dispersion from higher critical point oscillators at $E_1 = 1.6$ eV, $E_2 = 2.73$ eV, and $E_3 = 4.2$ eV. In contrast to previous studies, the dissipative and dispersive parts of the dielectric function *strictly* obey the Kramers-Kronig causality relations. Also, in this sense all level broadenings do not only appear in the imaginary part of the dielectric function, but cause corresponding energy shifts in its real part. An analytic formula of the complex dielectric function for the nonparabolic energy-momentum dispersion was derived within the framework of the six-band many-valley $k \cdot p$ model, and compared with the results of a corresponding parabolic model, keeping the oscillator strength and energy-level broadening identical. Only the dielectric function based on the nonparabolic band model correctly explains the observed transmission in the transparent regime below E_g and its steep decrease above the gap. It turns out that both the extinction coefficient as well as the refractive index of PbSe have considerably higher values than previously published. [S0163-1829(98)01004-2]

I. INTRODUCTION

IV–VI lead-salt semiconductor compounds (PbS, PbSe, PbTe) and their ternaries like $Pb_{1-x}Sn_xTe$, $Pb_{1-x}Sn_xSe$, $Pb_{1-x}Eu_xTe$, and $Pb_{1-x}Eu_xSe$, play an important role as midinfrared emitters and detectors in the wavelength range of 3–30 μm.[1–7] PbTe/$Pb_{1-x}Eu_xSe_yTe_{1-y}$ separate confinement buried heterostructure lasers hold the record for the highest cw operating temperature of 223 K in the midinfrared.[8] The highest *pulsed* operation temperature of 282 K was reported for a wavelength of 4.2 μm for a PbSe/$Pb_{1-x}Sr_xSe$ diode laser.[9] For the optimization of the resonator design, precise data on the optical constants are required. The elements like Eu, Mn, and Sr have gained a major importance since they provide a large tuneability of the energy gaps even for low concentrations. For lattice matching to the substrates quaternary compounds like $Pb_{1-x}Eu_xTe_{1-y}Se_y$ (Ref. 10) or $Pb_{1-x}Mn_xS_{1-y}Se_y$ (Ref. 11) have been used.

Lead salts exhibit properties which are unusual with respect to other semiconductors: they possess extremely high dielectric constants, a narrow direct fundamental band gap $E_g < 0.5$ eV at the L points of the Brillouin zone (BLZ) with a temperature coefficient $(dE_g/dT) > 0$. The photonic IV–VI compound devices benefit from the nearly mirror like many-valley conduction and valence bands with their comparatively high density-of-states (DOS) masses at the M_0 critical point. The band structure determines the dielectric function $\varepsilon(E)$, where $E = \hbar\omega$ denotes the photon energy, which determines the optical constants, i.e., the index of refraction $n(E)$ and extinction $k(E)$.[12–14]

So far derivations of the dielectric function of lead chalcogenides neglect band nonparabolicity effects for photon energies *near* the fundamental absorption edge. These were previously only taken into account for $E \geqslant 2E_g$ for highly doped samples or ternary samples like $Pb_{1-x}Sn_xTe$.[15,16] In these previous papers (i) the anisotropic multivalley structure of both conduction and valence bands, (ii) nonparabolic Kane-type energy dispersion, and (iii) **k**-dependent matrix elements are already accounted for. Some salient features like the rapid rise of the joint density of states with increasing photon energy in comparison to that following from a parabolic energy-momentum dispersion was correctly found, as well as the somewhat compensating influence of the energy-dependent reduction of the interband momentum matrix elements.[16] The primary objective was the calculation of the frequency-dependent absorption coefficient in terms of the joint density of states and an *average index of refraction*. The derivation of optical constants from a nonparabolic energy-momentum dispersion relation has been exemplified, e.g., for PbTe in Ref. 17. So far in the literature,[15–18] the analysis starts with a given functional dependence of the joint density of states $J_{cv}(\omega)$ between valence (v) and conduction (c) bands on the photon frequency ω, and continues with the calculation of the absorption $\alpha(\omega)$,

$$\alpha(\omega) = \frac{\omega\ \mathrm{Im}[\hat{\varepsilon}(\omega)]}{c_0\langle n\rangle} \propto \frac{\omega}{c_0\langle n\rangle}\left[\frac{J_{cv}(\omega)}{\omega^2}\right]. \qquad (1)$$

From $\alpha(\omega)$, the extinction $k(\omega)$ coefficient is derived:

$$k(\omega)=\frac{2c_0}{\omega}\,\alpha(\omega). \tag{2}$$

From the extinction $k(\omega)$ coefficient, via a Kramers-Kronig transformation, the frequency-dependent index of refraction $n(\omega)$ is determined. Equation (1) presumes a knowledge of the index of refraction *a priori*, whose frequency dependence is not known. It must be related by the causality (Kramers-Kronig) relations to the extinction coefficient $k(\omega)$—and in turn to the frequency dependence of $\alpha(\omega)$. To avoid violation of the causality principle, a constant *average* value of $n(\omega)$ is estimated. Reference 17 followed the same procedure: after calculating $k(\omega)$ from Eq. (2), a Kramers-Kronig transformation was applied to obtain the frequency-dependent $n(\omega)$. A subsequent self-consistency check of Eq. (1) by replacing $\langle n(\omega)\rangle$ through the *true* $n(\omega)$ was not performed. The Kramers-Kronig transformation was treated *numerically*. To some extent it suffered from the arbitrariness of the choice of the upper cutoff wave-number boundary used for integration.[17]

In this paper the inconsistencies quoted above are avoided, by the consequent use of Kramers-Kronig compatible optical constants, for which level broadening is included consistently. As an example, we use this formalism to analyze the optical transmission near the fundamental energy gap of epitaxial PbSe and $Pb_{1-x}Mn_xSe$ ($x\leqslant 0.013$) films grown by molecular-beam epitaxy[19] on (111) BaF_2 substrates at room temperature. We derive analytic expressions for the Kramers-Kronig pairs $\varepsilon_1(\omega)=\mathrm{Re}(\varepsilon)$ and $\varepsilon_2(\omega)=\mathrm{Im}(\varepsilon)$, comparing both the *parabolic* and the (more concise) *nonparabolic* $\mathbf{k}\cdot\mathbf{p}$ models. The correspondence of both models is worked out thoroughly in order to recover the malfications of the parabolic model with respect to the nonparabolic one.

Nonparabolicity corrections are required for a correct phase match of the Fabry-Perot thickness interferences in the *transparent regime* ($\hbar\omega<E_g$), and in addition a background dielectric function has to be considered as well. This nearly frequency-independent contribution arises from higher critical-point transitions in the bandstructure of PbSe,[20,21] which are introduced as *far-band oscillators* into the model dielectric function. In the notation of Cardona and Greenaway,[22] the dominant features for the background dielectric function of PbSe are the first shoulder $E_1=1.6$ eV, the highest peak oscillator $E_2=2.73$ eV, and a high-energy shoulder $E_3=4.1$ eV. We also use PbSe-related far-band oscillators, as quoted in Ref. 20, for a description of $Pb_{1-x}Mn_xSe$ samples, which seems to be justified for $x<0.013$. We rule out contributions from free-carrier absorption and phonons as being not relevant in the energy range of interest. They may be included by a two-term Sellmeier equation.[23,24]

The paper is organized as follows: In Sec. II an analytic derivation of the dielectric function of PbSe from either the parabolic or the nonparabolic six-band $\mathbf{k}\cdot\mathbf{p}$ model (with the inclusion of far-band corrections up to k^2),[25–27] and far-band oscillators at other critical points,[20] is presented. In Sec. III the frequency dependence of the optical constants is determined, and room-temperature transmission spectra of PbSe and $Pb_{1-x}Mn_xSe$ ($x\leqslant 0.013$) are fitted with the theory. All band parameters for PbSe and $Pb_{1-x}Mn_xSe$ were derived from magnetooptical experiments at low temperatures so far.[28–30] Thus for the room-temperature transmission data it is necessary to adjust two essential band parameters, namely, the energy gap and the oscillator strength, as well as the damping parameters and a background dielectric constant. In Sec. IV the competition between the parabolic and the nonparabolic dielectric function models are discussed, and the most convenient model is applied for an accurate determination of the x dependence of the energy gap of $Pb_{1-x}Mn_xSe$.

II. MODEL DIELECTRIC FUNCTION OF PBSE

In the $\mathbf{k}\cdot\mathbf{p}$ treatment according to Mitchell and Wallis for the lead salts,[26] the momentum-matrix elements between the L_6^- conduction band and L_6^+ valence band are kept as fixed quantities regardless of the magnitude of the energy gap (which changes, e.g., with temperature). In this approximation the enhancement of the transverse and longitudinal DOS masses is directly governed by the increase of E_g. Data on the band parameters (effective masses and momentum matrix elements) were collected with high accuracy in cyclotron resonance studies[28] and by optical four-wave mixing and coherent anti-stokes raman spectroscopy.[29,30]

The adjacent $|v\rangle=L_6^+$, $|c\rangle=L_6^-$ valence- and conduction-band levels correspond to the fundamental M_0 critical point. For finite wave vectors $\mathbf{k}$, they are strongly coupled in this approach using transverse and longitudinal momentum matrix elements ($\mathbf{P}_\perp$,$\mathbf{P}_\parallel$), which describe the *anisotropy* and *nonparabolicity* of the ellipsoidally shaped $E(k)$ relation at the L point of the BLZ. The far bands $L_{4,5}^+$, $L_{4,5}^-$ and L_6^+, L_6^- (levels of the same symmetry as the band-gap Bloch states $|v\rangle$ and $|c\rangle$) are treated up to second-order perturbation $E(\mathbf{k})\propto\mathbf{k}^2$. The proportionality factors can be represented as *far-band masses* m_l^+, m_l^-, m_t^+, and m_t^-. Again the superscripts $\pm$ label the valence- and conduction-band states, respectively. The anisotropy of the ellipsoidal constant energy surface is distinctly modified by these far-band contributions along the transverse (t) and longitudinal (l) directions with respect to the Γ-L direction of the star of $\mathbf{k}$ in the BLZ. Thus the energy-momentum dispersion can be finally expressed by the following band-edge masses at $\mathbf{k}=0$:

$$\frac{m_0}{M_\parallel^{+,-}}=\frac{2P_\parallel^2}{E_g m_0}+\frac{m_0}{m_l^{+,-}}, \tag{3}$$

$$\frac{m_0}{M_\perp^{+,-}}=\frac{2P_\perp^2}{E_g m_0}+\frac{m_0}{m_t^{+,-}}, \tag{4}$$

where m_0 is the free-electron mass. The DOS masses (which enter for all interband coupling and transition phenomena) are reduced masses of the hole mass in $|v\rangle$ and of the electron mass in $|c\rangle$:

$$\frac{1}{M_\perp}=\frac{1}{M_\perp^+}+\frac{1}{M_\perp^-}\quad(\text{transverse to }\Gamma\text{-}L), \tag{5}$$

$$\frac{1}{M_\parallel}=\frac{1}{M_\parallel^+}+\frac{1}{M_\parallel^-}\quad(\text{parallel to }\Gamma\text{-}L), \tag{6}$$

TABLE I. The band parameters of PbSe at 4.2 K.

E_g (meV)	$2P_\parallel^2/m_0$ (eV)	$2P_\perp^2/m_0$ (eV)	$\frac{m_t^-}{m_0}$	$\frac{m_l^-}{m_0}$	$\frac{m_t^+}{m_0}$	$\frac{m_l^+}{m_0}$
146.3	1.98	3.6	0.27	0.95	0.29	0.37

Since the band edge masses [Eqs. (3) and (4)] contain the far-band corrections, the DOS masses [Eqs. (5) and (6)] consist of both *mirrorlike* contributions from the (squared) momentum matrix elements $\mathbf{P}_\perp$ and $\mathbf{P}_\parallel$ (which do not select between labels + and −) and of far-band contributions different for both ± labels. The (nonparabolic and anisotropic) energy-momentum relation can be expressed in terms of these DOS masses and by the far-band masses[17]

$$E_{\mathrm{cv}}(k)=\frac{1}{2}\left[\frac{\hbar^2}{2}\left(\frac{1}{m_t^-}-\frac{1}{m_t^+}\right)k_\perp^2+\frac{\hbar^2}{2}\left(\frac{1}{m_\perp^-}-\frac{1}{m_\perp^+}\right)k_z^2\right] \pm\frac{E_g}{2}\left(1+\frac{\hbar^2k_\perp^2}{E_gM_\perp}+\frac{\hbar^2k_z^2}{E_gM_\parallel}\right)^{1/2}. \tag{7}$$

The upper (+) and lower (−) signs correspond to the conduction (c) and valence (v) bands, respectively. k_z and $k_\perp$ are the wave-vector components parallel and perpendicular to the Γ-L direction of a valley.

The root of Eq. (7) reflects the nonparabolicity of the bands. For small wave vectors—i.e., for terms in the root only slightly different from unity—expression (7) can be expanded. Then a *parabolic dispersion relation* for the conduction and valence bands emerges from formula (7):

$$E_c(k)=+\left(\frac{E_g}{2}+\frac{\hbar^2k_\perp^2}{2M_\perp^-}+\frac{\hbar^2k_z^2}{2M_\parallel^-}\right), \tag{8}$$

$$E_v(k)=-\left(\frac{E_g}{2}+\frac{\hbar^2k_\perp^2}{2M_\perp^+}+\frac{\hbar^2k_z^2}{2M_\parallel^+}\right). \tag{9}$$

If the far-band corrections are neglected, the DOS masses do not distinguish between ± labels, and hence the bands again become mirrorlike: $E_c(k)=-E_v(k)$. The band parameters and far-band masses of PbSe at $T=4.2$ K are given in Table I, and the effective masses and DOS masses in Table II.

The joint-density of states $J_{\mathrm{cv}}(E=\hbar\omega)$ connects a certain $|v\rangle$ state with the corresponding state in $|c\rangle$ at proper $\mathbf{k}$ vectors. $E(=\hbar\omega)$ is the photon energy in an absorption process. From Eqs. (7) and (8) we find, for the nonparabolic case,

$$E=E_c-E_v=E_s\left[1+\frac{\hbar^2k_\perp^2}{E_sM_\perp}+\frac{\hbar^2k_z^2}{E_sM_\parallel}\right]^{1/2}, \tag{10}$$

and, using definitions (5) and (6) for the parabolic case,

TABLE II. The effective masses and density-of-states masses of PbSe at 4.2 K.

$M_\parallel^-/m_0$	$M_\perp^-/m_0$	$M_\parallel^+/m_0$	$M_\perp^+/m_0$	$M_\parallel/m_0$	$M_\perp/m_0$
0.068	0.062	0.035	0.036	0.032	0.018

$$E=E_c-E_v=E_g+\frac{\hbar^2k_\perp^2}{2M_\perp}+\frac{\hbar^2k_z^2}{2M_\parallel}. \tag{11}$$

Both relations can be rewritten as ellipsoidal constant photon energy (E) surfaces in $\mathbf{k}$ space with principal axes a and b:

$$\frac{k_\perp^2}{a^2}+\frac{k_z^2}{b^2}=1, \tag{12}$$

$$\left.\begin{aligned}a^2&\equiv\frac{M_\perp}{\hbar^2E_g}(E^2-E_g^2)\\ b^2&\equiv\frac{M_\parallel}{\hbar^2E_g}(E^2-E_g^2)\end{aligned}\right\}\quad(\text{nonparabolic}), \tag{13}$$

$$\left.\begin{aligned}a^2&\equiv\frac{2M_\perp}{\hbar^2}(E-E_g)\\ b^2&\equiv\frac{2M_\parallel}{\hbar^2}(E-E_g)\end{aligned}\right\}\quad(\text{parabolic}). \tag{14}$$

The differential volume dV_k in $\mathbf{k}$ space between adjacent energy surfaces E, $E+dE$ can be calculated by differentiating the ellipsoid volume $V_k=4\pi a^2b/3$. The number of states per unit volume within dV_k is just the *joint density of states* $J_{\mathrm{cv}}(E)$:

$$dN(E)=\frac{1}{8\pi^3}\,dV_k=J_{\mathrm{cv}}(E)dE. \tag{15}$$

After some algebra, the explicit formulas for $J_{\mathrm{cv}}(E)$ are the following: for the nonparabolic case,

$$J_{\mathrm{cv}}(E)=\frac{M_\perp\sqrt{M_\parallel}}{2\pi^2\hbar^3E_g^{3/2}}E(E^2-E_g^2)^{1/2}: \tag{16}$$

and, for the parabolic one,

$$J_{\mathrm{cv}}(E)=\frac{M_\perp\sqrt{M_\parallel}}{\sqrt{2}\pi^2\hbar^3}(E-E_g)^{1/2}. \tag{17}$$

The *imaginary part of the dielectric function* is proportional to the joint density of states and to the electric dipole transition matrix element $|\overline{e\cdot p_{\mathrm{cv}}}|^2$, which in turn can be expressed by the corresponding interband momentum matrix elements $\mathbf{P}_\perp$ and $\mathbf{P}_\parallel$ for a given light polarization $\overline{e}$ with respect to the frame axes of the valley ellipsoid:

$$\mathrm{Im}(\varepsilon)=\frac{\pi e^2\hbar^2}{\varepsilon_0m_0^2E^2}|\overline{e\cdot p_{\mathrm{cv}}}|^2\cdot J_{\mathrm{cv}}(E). \tag{18}$$

One should notice that—apart from the photon energy, the transition matrix element, and the joint density of states—only universal quantities enter the expression Eq. (18). Due to the ellipticity of the energy dispersion and due to the many-valley character from equivalent center positions of the L points at the edge of the BLZ, a proper average over all valleys must be taken for the transition matrix element. For normal incidence on a (111) surface of PbTe and unpolarized light, the mean value of $|\overline{e\cdot p_{\mathrm{cv}}}|^2$ averaged over the

three oblique valleys and the one longitudinal (111) valley is evaluated in Appendix B of Ref. 17:

$$\langle|\overline{e\cdot p_{cv}}|^2\rangle = g_s g_\nu \frac{2P_\perp^2+P_\parallel^2}{3}, \tag{19}$$

where g_s is the spin-degeneracy factor ($g_s=2$), and g_ν the valley degeneracy ($g_v=4$). Previously,[17,18] a level broadening was introduced by convolving Im(ε) with a Lorentzian line-shape function $\Gamma(E)$. Afterwards a Kramers-Kronig transformation (KKT) was performed numerically to obtain Re(ε). This procedure suffers from imponderabilities due to the arbitrariness in selecting the upper-frequency cutoff in the numerical KKT.[17]

We follow the more straightforward procedure of deriving an *analytic* model dielectric function, as demonstrated in Ref. 31 for GaP, GaAs, InP, InAs, and InSb, and in Ref. 20 for PbSe. However, in these publications nonparabolicity for the M_0 critical point transition was neglected, and the higher critical points in the strongly absorbing regime were emphasized. By subjecting Im(ε) to an analytic KKT, Re(ε) was determined by evaluating the integral

$$\mathrm{Re}\{\varepsilon(E)\} = \frac{2}{\pi}\int_0^\infty \frac{E'\,\mathrm{Im}\{\varepsilon(E')\}}{E'^2-E^2}\,dE'. \tag{20}$$

Indeed, for a parabolic band dispersion at the M_0 critical point, Eq. (20) can be expressed in a closed form.[20,31] Level broadening (i.e., damping of the M_0 transition) is introduced *after* KKT, with the advantage of retaining the expressions in a closed analytic form. The photon energy E is continued in the complex plane by adding an imaginary damping parameter $i\Gamma$. Then the continued complex energy is inserted into the *real part* of the dielectric function,

$$E \rightarrow E + i\Gamma. \tag{21}$$

Replacing Im(ε) in Eq. (20) by the expression Eq. (18), and using Eqs. (17) and (19) for the parabolic case, we find, by integration for the complex dielectric function of PbSe near the M_0 critical-point transition, the following expression for the parabolic case:[20]

$$\hat{\varepsilon}(E) = \sqrt{2}A\left(\frac{E_g}{E+i\Gamma}\right)^2\left[2-\left(1+\frac{E+i\Gamma}{E_g}\right)^{1/2} - \left(1-\frac{E+i\Gamma}{E_g}\right)^{1/2}\right]. \tag{22}$$

The dimensionless parameter A is interpreted as the oscillator strength of the M_0 transition,

$$A = \frac{g_s g_v e^2}{2\pi\varepsilon_0 m_0^2\hbar}\frac{M_\perp\sqrt{M_\parallel}}{E_g^{3/2}}\frac{2P_\perp^2+P_\parallel^2}{3}. \tag{23}$$

Equation (22) is the same expression as derived for PbSe in Ref. 20, but with the essential refinement for the oscillator strength: an explicit dependence of the combined density-of-states mass on the valley anisotropy ($M_\parallel, M_\perp$) appears, and a valley degeneracy factor $g_\nu=4$ can be factorized out (for *unpolarized* light). Only in this case do all valleys (three oblique, one parallel to the [111] direction) contribute with equal parts to the average interband transition matrix element $(2P_\perp^2+P_\parallel^2)/3$. For polarized excitation, Eq. (23) has to be recalculated, correspondingly.

A comprehensive derivation of the optical properties from a *nonparabolic* energy-momentum dispersion near the M_0 critical-point transition following this procedure, as outlined above by evaluating Eq. (20), has not been performed to the best of our knowledge. We start with the imaginary part of the dielectric function Eq. (18), but take for the joint density of states the nonparabolic case, Eq. (16). Collecting the prefactors and introducing the oscillator strength A according to Eq. (23), we evaluate the KKT, Eq. (20),

$$\mathrm{Re}[\hat{\varepsilon}(E)] = \frac{2A}{\pi}\lim_{u\rightarrow\infty}\int_0^u \frac{(E'^2-E_g^2)^{1/2}}{(E'^2-E^2)}\,dE'. \tag{24}$$

The integration leads to

$$\mathrm{Re}[\hat{\varepsilon}(E)] = \frac{2A}{\pi}\lim_{u\rightarrow\infty}\left[\ln\frac{u+(u^2-E_g^2)^{1/2}}{(-E_g^2)}\right] - \frac{2A}{\pi}\frac{(E^2-E_g^2)^{1/2}}{E}\tanh^{-1}\left[\frac{E}{(E^2-E_g^2)^{1/2}}\right]. \tag{25}$$

Since we are interested in the *dispersion* of the dielectric function, only the second term reflects the energy dependence of Re(ε), which should be retained for the calculation of optical constants. The first part (which diverges in the limit) acts as of *frequency-independent* constant which can be included in ε_∞. Similarly, the higher interband transitions contribute to a constant (or weakly frequency dependent) background dielectric constant ε_∞ for the M_0 transition as well. Because we attempt to compare Eq. (25) with the parabolic one [Eq. (22)], we match both functions at $E=0$. With this constraint and taking $E\rightarrow E+i\Gamma$, we obtain the following complex dielectric functions for direct comparison: for the parabolic case,

$$\hat{\varepsilon}(\omega) = \varepsilon_\infty(E) + \sqrt{2}A\left(\frac{E_g}{E}\right)^2\left[2-\left(1+\frac{E}{E_g}\right)^{1/2}-\left(1-\frac{E}{E_g}\right)^{1/2}\right]; \tag{26}$$

and, for the nonparabolic one,

$$\hat{\varepsilon}(E) = \varepsilon_\infty(E) + A\left(\frac{1}{2\sqrt{2}}+\frac{2}{\pi}\right) - \frac{2A}{\pi}\frac{(E^2-E_g^2)^{1/2}}{E}\tanh^{-1}\left[\frac{E}{(E^2-E_g^2)^{1/2}}\right]. \tag{27}$$

$\varepsilon_\infty(E)$ includes all contributions from the higher E_1, E_2, and E_3 interband transitions in the notation of Refs. 20 and 22. The second term in Eq. (27) ensures that the dielectric functions [Eqs. (26) and (27)] are identical at $E=0$.

To complete the analysis, we take for $\varepsilon_\infty(E)$ the damped harmonic-oscillator contributions from the higher E_1 and E_2 transitions, and for the E_3 gap a two-dimensional M_0 critical point, as defined in Ref. 20:

TABLE III. Parameters of higher-energy critical-point transitions (far-band oscillators) of PbSe at room temperature, taken from Ref. 20.

E_1 (eV)	E_2 (eV)	E_3 (eV)	C_1	C_2	B	γ_1	γ_2	Γ_3 (meV)	ε_∞
1.6	2.73	4.1	3.5	15.4	1.2	0.0018[a]	0.0024[a]	1.5[a]	1.95[b]

[a]Value of Ref. 20 reduced by a factor of 5×10^{-3}.
[b]Replaces 1.5 of Ref. 20.

$$\hat{\varepsilon}_\infty(E)=\varepsilon_\infty+\frac{C_1E_1^2}{E_1^2-E^2-i\gamma_1E_1E}+\frac{C_2E_2^2}{E_2^2-E^2-i\gamma_2E_2E}-B\left(\frac{E_3}{E+i\Gamma_3}\right)^2\ln\left[1-\left(\frac{E+i\Gamma_3}{E_3}\right)^2\right]. \quad (28)$$

The energies E_i, oscillator strengths B and C_i, and damping parameters γ_i and Γ_3 are given in Table III.

With the complex dielectric functions derived from Eqs. (26)–(28), the optical constants $n(E)$ and $k(E)$ of PbSe can be calculated as usually performed in the dielectric theory of homogeneous media:

$$n(E)=\frac{1}{\sqrt{2}}\{[\mathrm{Re}^2(\hat{\varepsilon})+\mathrm{Im}^2(\hat{\varepsilon})]^{1/2}+\mathrm{Re}(\hat{\varepsilon})\}^{1/2}. \quad (29)$$

$$k(E)=\frac{1}{\sqrt{2}}\{[\mathrm{Re}^2(\hat{\varepsilon})+\mathrm{Im}^2(\hat{\varepsilon})]^{1/2}-\mathrm{Re}(\hat{\varepsilon})\}^{1/2}. \quad (30)$$

After the complex index of refraction $n+ik$ is determined by calculation, the transmission through an epitaxial layer grown on an insulating substrate (BaF_2) can be evaluated using the boundary conditions of fields across the interfaces of the two-layer system.[32] An efficient way of computing is the transfer-matrix method.[33] The optical constants of the PbSe film are taken from Eqs. (29) and (30), and the substrate (BaF_2) is assumed to be nonabsorbing in the frequency range of interest ($n_s=1.39$). The optical thickness (n_sd_s) of the substrate is so large that constructive interferences are only observed as ''thickness fringes'' from the film, but not from the substrate. To fit the experimental room temperature transmission spectra of PbSe and its related compounds $Pb_{1-x}Mn_xSe$ near the fundamental absorption edge four parameters enter the calculations: The oscillator strength A and energy gap E_g are essential parameters, and in addition the damping Γ and the background dielectric constant ε_∞. All remaining parameters are treated as fixed constants taken from Table III.

III. TRANSMISSION SPECTRA OF EPITAXIAL PbSe AND $Pb_{1-x}Mn_xSe$ FILMS

In the following we apply both the parabolic and nonparabolic model dielectric functions (including the far band oscillators) for the description of transmission spectra of PbSe and $Pb_{1-x}Mn_xSe$ ($x\leqslant0.013$) at $T=300$ K. The PbSe and $Pb_{1-x}Mn_xSe$ samples were grown by molecular-beam epitaxy on (111) BaF_2 substrates. The growth conditions were described in Ref. 19. The structural quality of the samples was checked by high-resolution x-ray diffraction and scanning electron microscopy. The Mn content of the $Pb_{1-x}Mn_xSe$ samples was determined independently by using Vegard's law.[11,19] The infrared transmission experiments were performed with a Bruker 113v Fourier transform infrared spectrometer.[17] In the experimental spectral range (from $E=124$ to 380 meV), the substrate material BaF_2 is essentially transparent. The transmission of the film is obtained by deviding the transmitted spectrum of a sample with the one of a bare BaF_2 specimen. The (relative) experimental accuracy for subsequent scans is better than 0.1%.

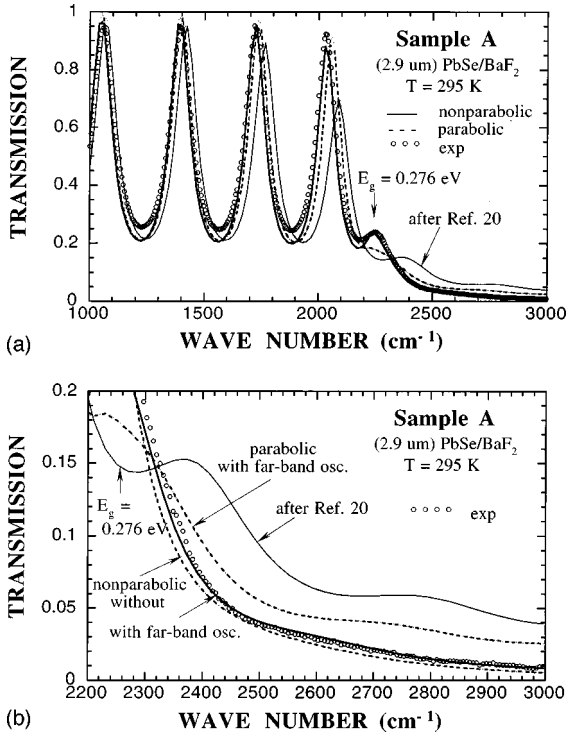

FIG. 1. Comparison of experimental transmission spectra (open dots) with calculations. Solid line: nonparabolic model; dashed line: parabolic model; second solid line: parabolic model using parameters from Ref. 20. (a) Overall spectrum, (b) magnified scale to rule out the parabolic models against the nonparabolic one. The influence of the energy dispersion from far-band oscillators at energies above 1.6 eV is shown in (b) by the lowest dashed curve, neglecting the dispersion, in comparison with those which incorporate such corrections (full and upper dotted line together with experimental data).

Figure 1 compares a measured transmission spectrum of sample A (2.9-μm-thick PbSe on BaF_2) with our calculations using the parabolic and nonparabolic model dielectric function. The *best* fit according to the *parabolic* model indicates insufficient coincidence with the experimental spectrum: below the band gap the thickness fringes [the dashed curve of Fig. 1(a)] exhibit an enhanced phase lag towards the absorption edge at 0.276 eV. This is a consequence of the smaller values of the index of refraction according to the parabolic model with respect to the nonparabolic one [see Fig. 2(a)]. Above the energy gap the absorption in the nonparabolic model is stronger [Fig. 1(b)] than in the parabolic limit.

We show also a transmission curve calculated for recently published data on the dielectric constants (Ref. 20). The essential discrepancies between our *parabolic* model fit and the

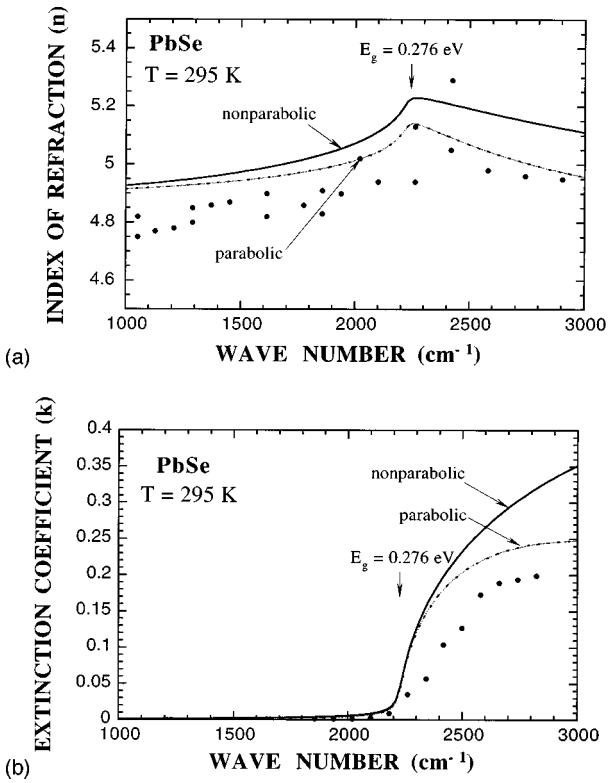

FIG. 2. (a) Index of refraction and (b) extinction coefficient of PbSe at $T=295$ K as a function of photon energy. The solid curves represent the nonparabolic dielectric function model, Eq. (27), the dashed curves the parabolic dielectric function model, Eq. (26), with identical oscillator strengths, dampings, and energy gaps. Published data from previous works are shown as black dots.

parabolic model of Ref. 20 result from different values for the oscillator strength A and damping parameters Γ, γ_1, γ_2, and Γ_3 (Tables III and IV). Since, after Ref. 20, the damping is much larger ($\Gamma=81$ cm^{-1}) the absorption edge is smeared out to a greater extent. Therefore the amplitude of the thickness fringes shrinks much more than experimentally observed for $E<E_g$, However, the larger damping leads to a higher transmission in the absorbing regime $E>E_g$. In Fig. 1(b) the influence of a residual dispersion from the far-band oscillators [Eq. (28)] on the nonparabolic model is demonstrated. If such a dispersion is neglected, Eq. (28) simplifies to

$$\hat{\varepsilon}_\infty(E)=\varepsilon_\infty+C_1+C_2+B=\text{const}. \tag{31}$$

The absence of the E dependence leads to a stronger curvature of the spectrum [lowest dashed curve in Fig. 1(b)], which is not observed in the experiment. The deviation from the full curve which fits the data excellently demonstrates the non-negligible influence of the dispersion of the damped oscillators far above the energy gap.

The photometric accuracy of our experimental transmission spectrum unambiguously rules out the parabolic model in favor to the nonparabolic one. The essential fitting parameters of the fundamental M_0 critical point-transition near E_g are summarized together with the corresponding data of $Pb_{1-x}Mn_xSe$ samples in Table IV.

Figure 2 shows the resulting index of refraction (a) and extinction (b) of PbSe from our fits to the transmission spectra (dashed and full lines) together with previously published data (black dots).[34] Especially for the index of refraction, a substantial scatter of the experimental data is evident. The cusp of the refractive index is rounded by finite damping ($\Gamma=18$ cm^{-1}), which is identical in both models. Note that from the common scaling condition of dielectric functions, both $n(E)$ curves converge to the same value at zero photon energy. The extinction coefficient [Fig. 2(b)] diverges in the nonparabolic model at high frequencies [which introduces mathematical divergences into the KKT for the frequency-independent part of Eq. (25)] whereas for the parabolic case it stays convergent in the entire frequency range. From the finite damping of the M_0 transition a residual absorption exists also for below-band-gap excitation.

Figure 3 shows the high photometric accuracy (0.1%) of the experimental transmission spectrum of PbSe in the absorbing spectral regime $E\geqslant E_g=2225$ cm^{-1}. Only the nonparabolic dielectric function yields a sufficiently accurate agreement with the experimental data. Deviations of the energy gap by more than 2 meV can be ruled out, since they lead to a fitting error larger than 0.001. Indeed, Fig. 3 demonstrates this fact by plotting calculated transmission spectra for $E_g=273$, 276, and 279 meV.

Finally we apply our model to an analysis of room-temperature transmission spectra of ternary $Pb_{1-x}Mn_xSe$ samples (B and C). The manganese concentration is within $0.007\leqslant x\leqslant 0.013$. For these small Mn contents, the energy-band scheme and the symmetry of critical points should re-

TABLE IV. Fit parameters of the model dielectric function to experimental transmission spectra of PbSe and $Pb_{1-x}Mn_xSe$ epitaxial layers of thickness d. The fitted oscillator strength A_{expt} is compared with theory according to Eq. (36) including the far-band correction K. Γ is the damping of the M_0 critical point transition at the energy gap E_g, and ε_∞ the background dielectric constant. To find coincidence with A_{expt}, a corresponding percentual increase (P%) of the momentum matrix elements as cited in Table I (e.g., for $2P_\perp^2/m_0$) must be anticipated.

Sample	x	d (μm)	E_g (eV)	Γ (cm^{-1})	A_{expt}	K	A_{theor}	P% (%)	ε_∞
A (PbSe)	0	2.9	0.276	18	5.4	0.70	6.1	28	1.95
B	0.007	4.9	0.294	30	5.0	0.68	5.9	39	2.05
C	0.013	2.8	0.316	30	4.7	0.67	5.8	52	0.84
#PbSe[a]	0	2.9[b]	0.276[c]	81			4.64		1.5

[a]Bulk PbSe sample with parameters taken from Ref. 20.

[b]For a comparison with our data in Fig. 1 we assumed the same thickness as for sample A.

[c]The original cited value from Ref. 20 was 0.31 eV, which would not fit our transmission spectrum.

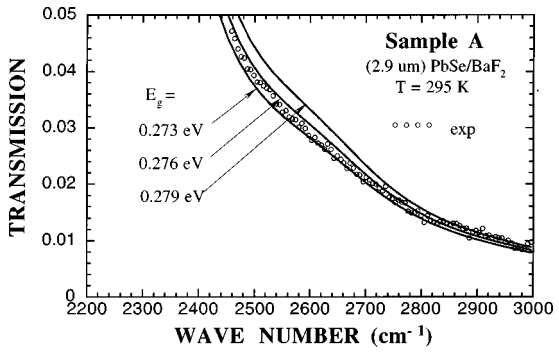

FIG. 3. Accuracy of our nonparabolic model fits: The plots for three values of E_g demonstrate that the energy gap of PbSe can be determined within an uncertainty of ± 2 meV.

semble the ones of PbSe. We assume that the momentum matrix elements are the same as for PbSe, and also the far-band masses and far-band oscillators. Then, by inspection of Eqs. (3) and (4), the band-edge masses depend only on the energy gap, which increases with Mn content. The transmission spectra together with model fits are given for samples $B(x=0.007)$ and $C(x=0.013)$ in Fig. 4. The spectrum of sample B shows a lower finesse of Fabry-Perot interference minima in the transparent spectral regime. This distinct appearance with respect to the other samples is assigned to a worse surface morphology of sample B. For this sample the density of cleavage steps was substantially higher than for the other samples A and C. Therefore the uniformity and flatness of the film layer is smaller for sample B. The parameters for the model dielectric function are summarized for the

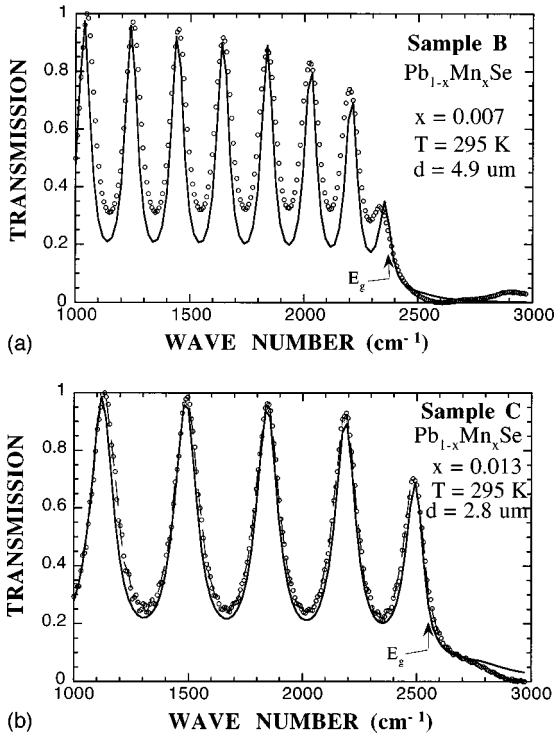

FIG. 4. Experimental transmission spectra of $Pb_{1-x}Mn_xSe$ epitaxial films ($x \leqslant 0.013$) on BaF_2 substrates together with model fits. The parameters of fits are given in Table IV.

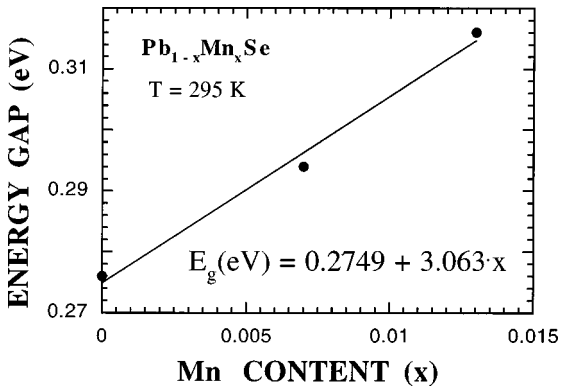

FIG. 5. The dependence of the fundamental absorption edge energy (E_g) as a function of manganese concentration of $Pb_{1-x}Mn_xSe$. The linear regression formula holds only for $T = 295$ K.

$Pb_{1-x}Mn_xSe$ samples in Table IV. The dependence of the energy gap of the $Pb_{1-x}Mn_xSe$ samples on the Mn content at room temperature is plotted in Fig. 5 together with a linear regression formula.

IV. DISCUSSION

The transmission spectra of the epitaxial layers, which were analyzed both in the transparent and absorbing regimes, exhibit a characteristic *phase shift* of the Fabry-Perot interferences toward $E=E_g$, which yields the energy dependence of the refractive index quite accurately. It turns out that this behavior of $n(\omega)$ can only be modeled by using a Kramers-Kronig-compatible index of refraction extracted from a dielectric function based on a model with *nonparabolic* energy-momentum dispersion. Since the thickness of the layers is determined independently, the analysis is governed essentially by two fitting parameters: the energy gap E_g and oscillator strength A. The former can be determined within ± 2 meV (see Fig. 3), the latter has to be compared with our theoretical predictions [Eq. (23)]. Most of the other parameters like damping factors and far-band oscillators are taken from literature with adjustments to our model. The findings from our nonparabolic dielectric function fits are summarized in Table IV. To facilitate the handling of Eq. (23) for the oscillator strength, we use a proper numerical expression using convenient energy units (eV) and effective masses in units of the free electron mass m_0 as given in Tables I and II.

$$A = 5.2 g_s g_v \frac{M_\perp/m_0 (M_\parallel/m_0)^{1/2}}{E_g[\mathrm{eV}]^{3/2}} \frac{1}{3} \left[2 \left(\frac{2P_\perp}{m_0} \right)^2 + \left(\frac{2P_\perp}{m_0} \right)^2 \right]_{[\mathrm{eV}]} . \tag{32}$$

We investigate the explicit influence of far-band contributions at the equivalent L points of the BLZ. The DOS masses [Eqs. (5) and (6)] are rewritten as a product of the two-band DOS masses $M_\perp$ and $M_\parallel$ and a correction factor due to the far bands:

$$\frac{1}{M_\perp}=\frac{4P_\perp^2}{m_0^2E_g}\left[1+\left(\frac{1}{m_1^+}+\frac{1}{m_1^-}\right)\frac{m_0^2E_g}{4P_\perp^2}\right]=\frac{1}{M_\perp^0}\left(1+\frac{M_\perp^0}{\mu_t}\right), \tag{33}$$

$$\frac{1}{M_\parallel}=\frac{4P_\parallel^2}{m_0^2E_g}\left[1+\left(\frac{1}{m_l^+}+\frac{1}{m_l^-}\right)\frac{m_0^2E_g}{4P_\parallel^2}\right]=\frac{1}{M_\parallel^0}\left(1+\frac{M_\parallel^0}{\mu_t}\right). \tag{34}$$

Reduced far-band masses (μ_l,μ_z) are introduced instead of the inner parentheses. Then the far-band correction for the joint-density-of-states mass which enters Eq. (32) takes the following simple form:

$$M_\perp\sqrt{M_\parallel}=M_\perp^0\sqrt{M_\parallel^0}\,\frac{1}{\left(1+\frac{M_\perp^0}{\mu_t}\right)\left(1+\frac{M_\parallel^0}{\mu_l}\right)^{1/2}}=M_\perp^0\sqrt{M_\parallel^0}K, \tag{35}$$

where the correction factor K represents the influence of far bands, and is a short notation for the fraction in Eq. (35). It is always smaller than unity, and is given in Table IV as well. The masses $M_\perp^0$ and $M_\parallel^0$ can also be expressed by the momentum matrix elements $P_\perp$ and $P_\parallel$, and the fundamental energy gap, and thus the oscillator strength Eq. (32) is represented by the three band parameters $P_\perp$, $P_\parallel$, and K:

$$A=1.8g_sg_v\frac{1}{3}\left[\frac{2\left(\frac{2P_\perp^2}{m_0}\right)+\left(\frac{2P_\parallel^2}{m_0}\right)}{\left(\frac{2P_\perp^2}{m_0}\right)\left(\frac{2P_\parallel^2}{m_0}\right)^{1/2}}\right]K. \tag{36}$$

All squares of momentum matrix elements in the parentheses are written in energy (eV) units. It should be noted that expression (36) holds only for constant, i.e., **k**-independent matrix elements and for unpolarized excitation ($g_v=4$, $g_s=2$). If the influence of the far bands can be neglected (μ_t, and μ_l are equal to infinity), $K=1$, and becomes independent of E_g as well. For $K=1$, the conduction and valence bands become mirrorlike, i.e., this corresponds to a two-band model. Thus, in this limit, for given values of the momentum matrix elements and fixed anisotropy, the oscillator strength does not vary with E_g and becomes independent of the x content of $Pb_{1-x}Mn_xSe$ samples.

With the aid of Eq. (36), a direct comparison with fits to the experimentally determined oscillator strength A_{expt} can be made, bearing in mind that the optical transmission experiments were performed at $T=300$ K. In Table IV, the oscillator strengths as obtained from a fit to transmission spectra and the values from the six-band $\mathbf{k}\cdot\mathbf{p}$ model ($K<1$) according to Eq. (36) are presented (however, based on the parameters obtained from low-temperature magneto-optical experiments, i.e., for $T<4.2$ K). It turns out that the calculated value A_{theor} always exceeds the observed value A_{expt}. Apparently the assumption of **k**- and E_g-independent matrix elements is not entirely justified. Generally, from inspection of Eq. (36) it follows that the momentum matrix elements should increase with increasing E_g, thus reducing the calculated oscillator strength A_{theor} in accordance with experiments.

To obtain agreement with the experimentally observed oscillator strengths at $T=300$ K, we have to increase the values of low-temperature momentum matrix elements $\mathbf{P}_\perp$ and $\mathbf{P}_\parallel$. This is done by multiplying their squared values as given in Table I, by a factor $(1+P\%/100)$, however, keeping the anisotropy $\mathbf{P}_\perp/\mathbf{P}_\parallel$ constant. The required percentual increase $P\%$ is shown in Table IV for our samples $A-C$. Furthermore, it should also be emphasized that more isotropic momentum matrix elements decrease the value of the oscillator strength A_{theor}.

Finally we comment on the damping parameters γ_1, γ_2, and Γ_3 (Table III) of the far-band oscillators at $E_1=1.6$, $E_2=2.73$, and $E_3=4.1$ eV. These transition energies were kept constant for PbSe as well as for $Pb_{1-x}Mn_xSe$ using the values given in Ref. 20. However, the damping parameters of the simple harmonic oscillators describing the higher critical points were reduced drastically with respect to the values given in Ref. 20. The reason for this behavior is the fact that over a wide frequency range a simple harmonic-oscillator model for the higher critical point transitions E_1, E_2, and E_3 does not describe the dielectric response properly at $E=E_g$. The reduction of the damping parameters for frequencies close to the fundamental gap was necessary to obtain good agreement for the Fabry-Perot fringes of the transmission spectra below the energy gap. Thus a rather strong dispersion of $\varepsilon_\infty(E)$ is necessary to describe correctly the low-energy transitions ($E<E_g$).

In summary, we developed a dielectric function model for optical interband transitions near the fundamental energy gap for IV-VI many-valley semiconductors, with specific applications to PbSe and $Pb_{1-x}Mn_xSe$ at room temperature. In the framework of a six-band $\mathbf{k}\cdot\mathbf{p}$ model, the nonparabolic energy-momentum dispersion has been proven to be the only realistic model which is consistent with experimental data. The dielectric functions were developed as *analytic* expressions for both parabolic and nonparabolic models with a common expression for the oscillator strength. Their real and imaginary parts indeed obey the causality principle, in contrast to previous studies. The number of fit parameters was kept to a minimum; only the energy gap, oscillator strength, and damping were modeled to fit the transmission spectra. Harmonic far-band oscillators—particularly important for exploring spectroscopic ellipsometry in the strongly absorbing regime—were adopted from recently published data with a modification of damping parameters, which brought excellent agreement with the observed transmission spectra of the epitaxial layers, even down to frequencies below the fundamental gap.

ACKNOWLEDGMENTS

We thank H. Straub for the SEM measurement of the thickness of the samples, and acknowledge financial support by the Österreichischer Fonds zur Förderung der wiss. Forschung under Grant No. 11557.

*Permanent address: Department of Electronic Materials Engineering, Research School of Physical Sciences and Engineering, Australian National University, Canberra, ACT 0200, Australia.

[1] D. L. Partin, IEEE J. Quantum Electronics **QE24**, 1716 (1988), and references therein.

[2] A. Ishida, H. Takashiba, T. Izutu, H. Fujiyasu, and H. Böttner, J. Appl. Phys. **75**, 619 (1994).

[3] H. Zogg, A. Fach, C. Maissen, J. Masek, and S. Blunier, Opt. Eng. (Bellingham) **33**, 1440 (1994).

[4] H. Zogg, A. Fach, J. John, J. Masek, P. Müller, C. Paglino, and S. Blunier, Opt. Eng. (Bellingham) **34**, 1946 (1995).

[5] A. Katzir, R. Rosman, Y. Shani, K. H. Bachem, H. Böttner, and H. M. Preier, in *Handbook of Solid State Lasers*, edited by P. K. Cheo (Marcel Dekker, New York, 1989), p. 228.

[6] M. Tacke, Infrared Phys. Technol. **36**, 447 (1995).

[7] H. Preier, Semicond. Sci. Technol. **5**, S12 (1990).

[8] Z. Feit, M. McDonald, R. J. Woods, V. Archambault, and P. Mak, Appl. Phys. Lett. **68**, 738 (1996).

[9] Z. Shi, M. Tacke, A. Lambrecht, and H. Böttner, Appl. Phys. Lett. **66**, 2537 (1995).

[10] G. Bauer, M. Kriechbaum, Z. Shi, and M. Tacke, J. Nonlinear Opt. Phys. Mater. **4**, 283 (1995).

[11] N. Koguchi, S. Takahashi, and T. Kiyosawa, Jpn. J. Appl. Phys. **27**, L2376 (1988).

[12] F. Stern, Phys. Rev. **133**, A1653 (1964).

[13] W. G. Opyd, Master's thesis, Naval postgraduate school, Monterey, CA, 1973.

[14] W. W. Anderson, IEEE J. Quantum Electron. **QE13**, 532 (1977).

[15] I. A. Drabkin, L. Ya. Morgovskii, I. V. Nel'son, and Yu. I. Ravich, Fiz. Tekh. Poluprovodn. **6**, 1323 (1992) [Sov. Phys. Semicond. **6**, 1156 (1973).]

[16] D. Genzow, K. H. Herrmann, H. Kostial, I. Rechenberg, and A. E. Yunovich, Phys. Status Solidi B **86**, K21 (1978).

[17] S. Yuan, H. Krenn, G. Springholz, and G. Bauer, Phys. Rev. B **47**, 7213 (1993).

[18] A. R. Forouhi and I. Bloomer, Phys. Rev. B **38**, 1865 (1988).

[19] N. Frank, A. Voiticek, H. Clemens, A. Holzinger, and G. Bauer, J. Cryst. Growth **126**, 293 (1993).

[20] N. Suzuki, K. Sawai, and S. Adachi, J. Appl. Phys. **77**, 1249 (1995).

[21] G. Martinez, M. Schlüter, and L. Cohen, Phys. Rev. B **11**, 651 (1975).

[22] M. Cardona and D. L. Greenaway, Phys. Rev. **133**, A1685 (1964).

[23] K. H. Herrmann and A. F. Rudolph, Infrared Phys. **33**, 63 (1992).

[24] A. R. Forouhi and I. Bloomer, in *Handbook of Optical Constants of Solids II*, edited by E. D. Palik (Academic, Boston, 1991), p. 151.

[25] E. O. Kane, Phys. Rev. **146**, 558 (1966).

[26] D. L. Mitchell and R. F. Wallis, Phys. Rev. **151**, 581 (1966).

[27] M. S. Adler, C. R. Hewes, and S. Senturia, Phys. Rev. B **7**, 5186 (1973); **7**, 5195 (1973).

[28] H. Burkhard, G. Bauer, and W. Zawadzki, Phys. Rev. B **19**, 5149 (1979).

[29] H. Pascher, Appl. Phys. B: Photophys. Laser Chem. **34**, 107 (1984).

[30] H. Pascher, G. Bauer, and R. Grisar, Phys. Rev. B **38**, 3383 (1988); F. Geist, H. Pascher, N. Frank, and G. Bauer, *ibid.* **53**, 3820 (1996).

[31] S. Adachi, Phys. Rev. B **35**, 7454 (1987).

[32] B. Harbecke, B. Heinz, V. Offermann, and W. Thei, in *Optical Characterization of Epitaxial Semiconductor Layers*, edited by G. Bauer and W. Richter (Springer, Berlin, 1996), p. 203.

[33] A. F. Terzis, X. C. Liu, A. Petrou, B. D. McCombe, M. Dutta, H. Shen, Doran D. Smith, M. W. Cole, M. Taysing-Lara, and P. G. Newman, J. Appl. Phys. **67**, 2501 (1990).

[34] G. Bauer and H. Krenn, in *Handbook of Optical Constants of Solids*, edited by E. D. Palik (Academic, New York, 1985), p. 517, and references therein.